The Journal of Green Energy and Environmental Engineering

Research Paper

Synthesis and Adsorption-Photocatalytic Properties of ZnO/Biochar Composites

Jerzy Jaroniec[1], Ilknur Balogh[2,*]

[1] Department of Chemistry and Biochemistry, Kent State University, Kent, 44-242, OH, USA
[2] Department of Chemical and Biological Engineering, Koc University, Rumelifeneri Yolu, Sariyer, 34450 Istanbul, Turkey
*Corresponding author: Ilknur.balogh@ku.edu.kr

Abstract. This study designed and constructed novel ZnO/NOC-based composite photocatalytic materials (ZnO/NOC, Cu@ZnO/NOC, Sn@ZnO/NOC) by leveraging the advantages of biochar, such as its large specific surface area and abundant pore structure. Various advanced characterization techniques were employed to investigate the synergistic effects between components, microstructure, electrical conductivity, and optical properties of the composites, and their UV and visible light photocatalytic activities were evaluated. Furthermore, the photocatalytic reaction mechanism was explored. Under solvothermal-calcination conditions (ethanol solvent, 700 °C, biomass/Zn mass ratio 0.30), the peanut-shell-derived ZnO/NOC composite delivered the highest combined adsorption and UV–vis photocatalytic activity. For instance, under UV light (300W Hg lamp), this ZnO/NOC composite achieved a degradation and decolorization rate of over 99.30% for the pollutant methylene blue (MB). Based on the ZnO/NOC composite, Cu and Sn were introduced to prepare two additional series of composites: Cu@ZnO/NOC and Sn@ZnO/NOC. The results indicated that under a calcination temperature of 700°C and a mass ratio of 0.30, the composites prepared with Cu-ZnO and Sn-ZnO molar ratios of 9.0% exhibited the best adsorption-photocatalytic performance. Comparing the three series (ZnO/NOC, Cu@ZnO/NOC, and Sn@ZnO/NOC), all demonstrated excellent adsorption and UV-visible light photocatalytic performance for pollutants. The performance was further improved due to the introduction of Cu and Sn, fully indicating that multi-component composition can effectively enhance material properties.

Keywords: *Biochar; Composite material; Dye; Adsorption; Photocatalysis*

Received on 02 April 2024, Accepted on 28 June 2024, Published on 15 July 2024

1 Introduction

In recent years, with the continuous advancement of global urbanization and industrialization and rapid economic development, environmental pollution and energy shortage have become increasingly prominent issues, posing urgent challenges [1]. Various persistent organic pollutants from industrial papermaking, textile industries, tanneries, and residual dyes after their use enter natural water resources, posing a severe threat to water quality [2]. Based on an in-depth understanding of organic dyes and their physical and chemical properties, conventional methods struggle to degrade their structures, necessitating the search for an efficient, simple, economical, and environmentally friendly treatment technology [4]. Photocatalytic reaction was discovered in an experiment where water was split into oxygen and hydrogen when a titanium oxide single crystal was placed in water under UV light irradiation [5]. It was found that the presence of a photocatalyst accelerates the catalytic process without itself participating in the chemical reaction; it is a substance that undergoes a chemical reaction due to photon excitation, thereby acting as a catalyst. Illumination promotes electrons from the valence band to the conduction band, generating strongly reducing photoelectrons that can reduce species adsorbed on the

catalyst surface [6]. Simultaneously, holes formed in the VB of the catalyst possess oxidizing ability and undergo oxidation reactions [7]. Therefore, photocatalytic reactions utilize catalysts to absorb photons, generate photogenerated electron-hole (e^--h^+) pairs, and carry out redox reactions to degrade organic compounds, converting light energy into chemical energy. This method offers simplicity of operation, mild conditions, high degradation efficiency, reusability, high utilization of solar energy, and broad application range, capable of treating various pollutants, making it one of the most effective methods for removing pollutants from water [8]. Consequently, photocatalytic degradation has quietly become a popular method for treating pollutants in water bodies, and photocatalytic technology has become a favored wastewater treatment approach [9].

Common traditional photocatalysts include semiconductors such as titanium dioxide (TiO_2) [10], zinc oxide (ZnO) [11], nickel oxide (NiO) [12], cadmium sulfide (CdS) [13], iron oxide (Fe_2O_3) [14], cuprous oxide (Cu_2O) [15], and graphene [16]. In recent years, with in-depth research on ZnO, its synthesis methods have gradually matured, including sol-gel, co-precipitation, solvothermal, and electrochemical deposition. The solvothermal method involves dissolving reactants in a solvent to form a homogeneous solution, placing it in an autoclave to create a closed system. At high temperatures, the reactants exist in a more reactive state, and as the temperature increases, chemical reactions occur slowly, generating the target product. This method allows control over the material's phase composition, particle size, and microstructure under high pressure and appropriate temperature. Furthermore, being in a closed system, it provides good dispersion, effectively preventing agglomeration, evaporation of toxic solvents, and oxidation of precursors [17]. Thus, this method is widely used for controlling particle size and morphology, easily yielding products with uniform size and controllable particle size. For example, some researchers [18] synthesized Tb-doped ZnO nanoparticles with sizes of 20–90 nm via the solvothermal method. The composite displays narrow size dispersion and a distinctive morphology; Tb incorporation into the ZnO lattice, confirmed by characterization and activity tests, markedly improves electron–hole separation and overall photocatalytic efficiency. Other researchers [19] used the solvothermal method to synthesize uniformly shaped Cu_2O spherical nanoparticles with sizes around 60 nm. Further coupling with ZnO formed a heterostructured nanomaterial with special morphology and uniform particle size. Photocatalytic experiments showed that the composite not only had high photocatalytic efficiency but also excellent reusability, indicating potential applications in wastewater treatment.

ZnO is favored by researchers due to its low cost, low toxicity, and stability. However, its wide bandgap limits its response to UV light, hindering widespread application [20]. To overcome this, strategies such as noble metal deposition, ion doping, microstructure 调控, semiconductor coupling, and carbon-based material compositing have shown progress. Among these, carbon-based material compositing is a common modification strategy. Common carbon materials include graphite, graphene oxide, and biomass. Graphite is often used in electrochemical deposition [21], but its preparation is complex. Graphene oxide possesses an ordered lattice and high surface area, yet its feedstock is non-renewable petroleum. Biomass is an environmentally friendly, green new material with advantages like large specific surface area, sustainability, and wide availability, finding extensive applications in photocatalysis [22]. Therefore, considering these characteristics, some researchers used biomass (pecan shell) as the carbon material and ZnO as the main active species to prepare a composite material (N20Z) [23]. The presence of biochar effectively increased the specific surface area, added active sites, and the black color enhanced light absorption. Under UV light, the composite achieved 100% removal of R97. This indicates that compositing ZnO with biomass can effectively enhance its photocatalytic activity. Thus, this modification strategy is environmentally friendly, economical, efficient, and feasible for modifying ZnO.

This paper uses biochar as a template, carbon source, and reducing agent, and zinc nitrate hexahydrate as the Zn source. ZnO/NOC, Cu@ZnO/NOC, and Sn@ZnO/NOC composites were prepared via the solvothermal-calcination method, and their photocatalytic performances were studied. First, the ZnO/NOC composite was prepared by a simple solvothermal-calcination method. Its physicochemical properties were characterized using XRD, SEM, IR, BET, XPS, TPR, PL, etc., and its visible light photocatalytic performance was evaluated under a 350W Xe lamp. Secondly, new components were introduced to investigate the effects of preparation conditions on phase composition, microstructure, and the photocatalytic performance against dyes, antibiotics, and under different light sources.

2 Materials and methods

2.1 Synthesis of ZnO/NOC Composite

The ZnO/NOC composite was prepared by the solvothermal-calcination method. $Zn(NO_3)_2 \cdot 6H_2O$ (3.6560 g) and glacial acetic acid (2.00 mL) were dissolved in 40.00 mL ethanol to afford an acidic medium; pre-treated biomass was then suspended in this solution and stirred for 24 h to ensure uniform dispersion.The slurry was sealed in an autoclave and solvothermally treated at 180 °C for 12 h. After drying at 80 °C, the solid was transferred to a tube furnace, heated at 5 °C min^{-1} under N_2 to 600–800 °C, and held for 2 h. By systematically varying both the final temperature and the biomass-to-ZnO mass ratio (0.0–0.5), a series of ZnO/NOC composites was obtained.

2.2 Preparation of Cu@ZnO/NOC Samples

High-performance Cu@ZnO/NOC was synthesized via a solvothermal-calcination route. Calcination temperature (600–800 °C) and biomass mass ratio (0.1–0.5) were first optimized; subsequently, the Cu/ZnO molar ratio was tuned from 0–15 % to yield the final Cu@ZnO/NOC series.

2.3 Preparation of Sn@ZnO/NOC Composite

The calcination temperature (600–800°C) and the biomass-to-metal mass ratio for composite preparation were optimized. Photocatalytic experiments showed that under a calcination temperature of 700°C and a biomass mass ratio of 0.30, the effect of the Sn^0-to-ZnO molar ratio on the composite was investigated.

$Zn(NO_3)_2 \cdot 6H_2O$ was used as the zinc source, $SnCl_4 \cdot 5H_2O$ as the tin source, and pretreated biomass as the carrier, carbon source, and reducing agent. Stoichiometric $Zn(NO_3)_2 \cdot 6H_2O$, $SnCl_4 \cdot 5H_2O$, 2.00 mL glacial acetic acid and biomass were dispersed in ethanol and stirred for 12 h to achieve homogeneous anchoring of Zn^{2+} and Sn^{4+} onto the substrate, after which the mixture was transferred to an autoclave and solvothermally treated at 180 °C for 12 h. The resulting precursor was dried at 80 °C; its darker hue relative to the raw biomass confirmed partial carbonization during solvothermal treatment. The solid was then calcined at 700 °C for 2 h under N_2 (5 °C min^{-1} ramp) to yield the final product.

2.4 Material Characterization and Analysis Methods

FT-IR spectra were recorded on a USA-made FTS3000FX spectrometer to identify surface functional groups. Samples were mixed with KBr (100:1 ratio), ground, and pressed into pellets.

XRD patterns were collected on a Rigaku D/Max-2400 diffractometer (Japan) with Cu Kα radiation (λ = 0.15418 nm) operated at 40 kV and 100 mA to determine phase composition and crystallinity.

Raman Spectroscopy: Carbon components were analyzed using a WITec alpha300RA+ Raman spectrometer (Germany).

Morphology, particle size, and surface elemental composition were examined with a JSM-6701F SEM and a JEM-2100 TEM (JEOL, Japan). Specimens were ultrasonicated in ethanol, deposited on copper grids, and dried prior to observation.

X-ray Photoelectron Spectroscopy (XPS): Chemical states of elements were determined using an AXIS SUPRA spectrometer. The C 1s peak at 284.6 eV was used for calibration.

BET Surface Area Analysis: Surface area together with pore-size distribution were evaluated with a TriStar II 3020 instrument at liquid-nitrogen temperature (77.35 K).

Electrochemical Analysis: A 10 mg portion of the powder was suspended in 0.5 mL H_2O, 0.5 mL EtOH and 2 µL Nafion®, sonicated, and 3 µL of the resulting ink was cast on a mirror-polished glassy-carbon substrate and air-dried. CV and EIS measurements were subsequently carried out with a CHI 660E potentiostat.

Optical Analysis: Optical properties were characterized using an F98 photoluminescence spectrometer (Lengguang), a UV-3600 Plus UV-Vis spectrophotometer (Japan), and a 752N Plus UV-Vis spectrophotometer (Shanghai Analysis Instrument Co., China).

2.5 Photocatalytic Performance Test

Four model contaminants—methylene blue, methyl violet, methyl orange, and tetracycline hydrochloride—were selected to probe photocatalytic activity under both UV and visible illumination supplied by a 300 W mercury source. In a standard run, 40 mg of photocatalyst was dispersed in 40 mL of dye stock of known concentration. The suspension was magnetically stirred for 30 min in the dark to establish adsorption equilibrium, after which illumination was started. At preset time points, 4 mL aliquots were withdrawn, immediately centrifuged to separate solids, and the absorbance of the clear supernatant was read at the respective λ_max: 664 nm for MB, 580 nm for MV, 460 nm for MO, and 356 nm for TC. The decolourisation ratio D_t was then computed as:

$$D_t = [1 - A_t/A_o] \times 100\%$$

where t denotes illumination time, A_o is the initial absorbance, and A_t the absorbance recorded after t min. Degradation kinetics were fitted to the pseudo-first-order expression $\ln(C_o/C_t) = k_1t$..

3 Results and discussion

3.1 XRD Analysis

X-ray diffraction was employed to probe phase make-up and lattice order. Patterns of T-600, T-700 and T-800 (Fig. 1a) display reflections at 31.4°, 34.1°, 36.2°, 48.1°, 57.6°, 64.2° and 69.6° 2θ, indexing to the (100), (002), (101), (102), (110), (103) and (112) planes of hexagonal wurtzite ZnO (JCPDS 36-1451). Peak sharpening with higher calcination temperature signals improved crystallinity. A subtle shift of the 36.2° reflection toward lower 2θ was also detected, revealing lattice expansion and distortion in ZnO, most likely induced by intimate contact with the NOC matrix. Absence of any NOC-related signals implies that ZnO growth delaminates the carbon layers and suppresses their long-range order. In the C-modified series A-0.0–0.5 (Fig. 1b), carbon incorporation leaves the wurtzite phase unchanged yet modulates its perfection. Peak height rises with increasing PS/ZnO mass ratio until ~0.30, where optimum ordering is achieved; beyond this threshold, further carbon depresses crystallinity. The bell-shaped trend in crystallinity can be rationalized by nucleation density. At low biomass loadings, the carbon surface becomes crowded with ZnO nuclei; their close proximity limits subsequent oriented growth and yields poorer ordering. Conversely, excessive biomass dilutes the precursor, producing widely separated nuclei that are too distant to sustain cooperative growth, again resulting in diminished crystal perfection. Therefore, only by adding an appropriate amount of biomass can an appropriate number of ZnO nuclei be formed on the biomass surface, allowing for directional growth of ZnO nuclei to obtain composites with higher crystallinity [26-27].

Next, a detailed analysis was conducted on the XRD patterns of the CuZ/NOC-0.0%~15.0% series. From the figure (Fig. 1c), it can be seen that diffraction peaks of Cu^0 and ZnO appeared in all samples. Compared to CuZ/NOC-0.0%, the crystallinity of the composites significantly improved after the addition of Cu metal.

Figure 1d shows the XRD patterns of samples SZ/NOC-0.0%~15.0% prepared under different "molar ratio" conditions. It can be found that within the studied "molar ratio" range, the introduction of Sn significantly improved the crystallinity of ZnO in the composites, i.e., the presence of $Sn^0/^{4+}$ was conducive to the directional growth of ZnO nuclei; and the crystallinity first increased and then decreased with increasing "molar ratio", reaching the best at approximately 9.0%. However, observation of the Sn^0 diffraction peaks revealed that with increasing Sn-ZnO "molar ratio", the intensity of the Sn^0 diffraction peaks (i.e., the content in the composite) first increased, reached a maximum at about 9.0%, and then gradually decreased. During the calcination process, sublimation of Sn^0 was observed, and the vaporization phenomenon became more obvious with increasing ratio, thus reducing the Sn^0 content in the material [28].

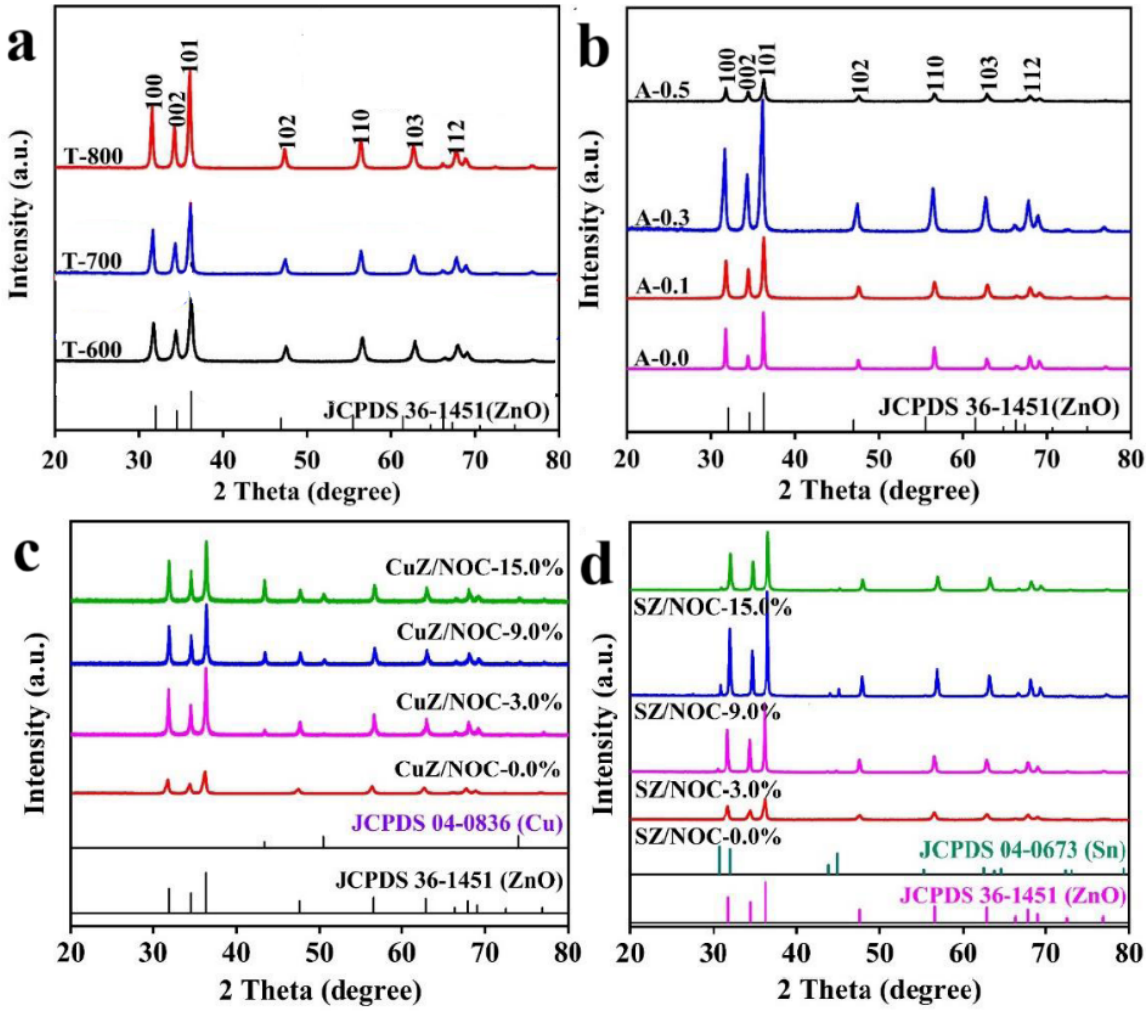

Figure 1 XRD spectra of samples

3.2 Raman Analysis

Because A-0.3(T-700) delivered the optimum adsorption-photocatalytic response, it was chosen for deeper structural and morphological scrutiny. Raman spectra of C-700 and T-700 are compared in Fig. 2a. The D band stems from A_1g symmetry phonons activated near the K-point, whereas the G band arises from zone-center E_2g vibrations within sp^2-hybridized carbon networks. The extent of graphitization in carbon scaffolds is commonly gauged through the I_D/I_G intensity ratio. For both C-700 and T-700, the D and G signatures appear at 1340 cm^{-1} and 1580 cm^{-1}, yielding I_D/I_G values of 1.05 and 1.11, respectively. These ratios confirm the presence of graphitic domains; the slightly higher value for T-700 points to a greater abundance of structural defects and a more pronounced degree of graphitization relative to its C-700 counterpart.

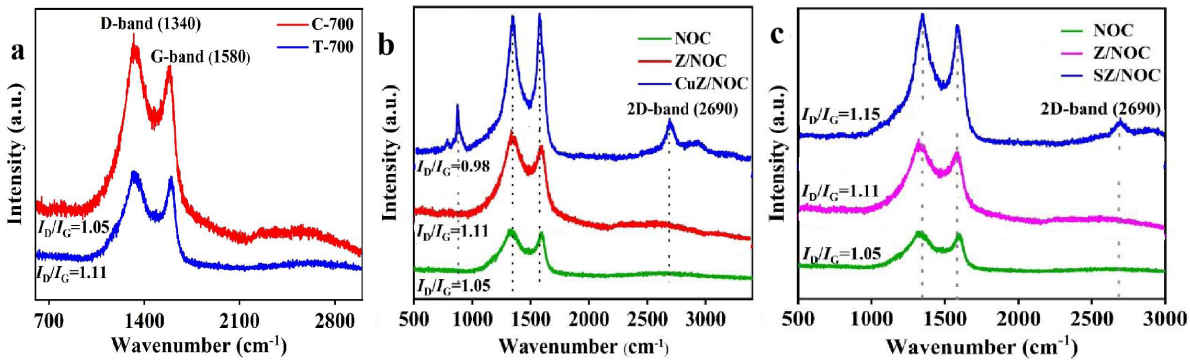

Figure 2 Raman spectra of samples

Owing to the biochar content, the carbonaceous domains were scrutinized by Raman spectroscopy (Fig. 2b). The D band originates from A_1g phonons near the K-point, whereas the G band reflects zone-center E_2g vibrations of sp^2-hybridized carbon. The I_D/I_G ratio is routinely adopted to quantify graphitization [29,30]; a value approaching unity signals a well-graphitized network. All samples exhibit D and G peaks centered at 1340 cm^{-1} and 1580 cm^{-1}, with I_D/I_G = 1.05 (NOC), 1.11 (Z/NOC), and 0.98 (CuZ/NOC), indicating that the NOC scaffold is highly graphitic and that Cu incorporation slightly enhances ordering.The ratio of sample CuZ/NOC was closer to 1, indicating that the carbon components in the formed material were graphitized. Furthermore, the intensity of the G band of material CuZ/NOC was greater than that of NOC and Z/NOC, indicating a more significant degree of graphitization. Therefore, it can be considered that the introduction of Cu promoted the graphitization degree of the material. Additionally, a signal peak appeared near 2690 cm^{-1}, indicating that the number of layers of the graphitic-like biochar carbon component changed from single-layer to multi-layer after carbonization. Therefore, incorporating Cu facilitates biomass pyrolysis, raises the carbon graphitization level, converts single carbon sheets into multilayer stacks and, consequently, enlarges the specific surface area—all factors that favor photocatalytic performance.

Raman technology was used to characterize the C components in the composites [31]. Figure 2c shows the Raman spectra of samples NOC, Z/NOC, and SZ/NOC. "Combined with XRD results, it can be seen that ZnO and Sn metal phases exist in the composites. Below, Raman technology is used to further discuss the carbon components of the composites." Comparison of the Raman fingerprints reveals I_D/I_G ratios of 1.05 for NOC, 1.11 for Z/NOC, and 1.15 for SZ/NOC, confirming that the carbon frameworks in all three architectures are graphitic. Furthermore, SZ/NOC had a larger I_D/I_G value than NOC and Z/NOC, indicating that the material contained abundant structural defects. Hence, Sn exerts a stronger influence than Cu on both the graphitization extent and the density of structural defects within the carbon matrix. Secondly, a significant signal peak also appeared near 2690 cm^{-1} for the SZ/NOC composite, indicating that the graphitic carbon layers were multi-layered. Based on the above conclusions, it is speculated here that the metal and ZnO nanoparticles can exfoliate the carbon layers into multi-layer graphene layers, with the metal playing a more significant role.

3.3 XPS Analysis

The surface chemistry of the optimal A-0.3(T-700) specimen was probed by XPS [32]. The survey scan (Fig. 3a1) confirms the coexistence of C, N, O and Zn. High-resolution C 1s emission (Fig. 3a2) displays components at 284.6 eV (graphitic C=C) and 287.9 eV (C–N→Zn linkage). The O 1s envelope (Fig. 3a4) is resolved into 530.9 eV (Zn–O–Zn lattice oxygen) and 532.6 eV (C–O–Zn interfacial oxygen). In the N 1s spectrum (Fig. 3a3), it can be fitted into three peaks at 398.4 eV, 399.4 eV, and 400.9 eV [33], corresponding to pyridinic N, pyrrolic N, and graphitic N, respectively. High-resolution Zn 2p data for A-0.0 (Fig. 3a5) exhibit spin–orbit-split peaks at 1021.4 eV (Zn $2p_3/_2$) and 1044.5 eV (Zn $2p_1/_2$), separated by 23.1 eV—fingerprinting Zn^{2+}. An identical doublet is observed for A-0.3, confirming the divalent oxidation state remains unchanged after carbon incorporation. Remarkably, the Zn 2p doublet of A-0.3 is displaced +0.8 eV relative to bare ZnO, signalling diminished electron density around Zn centres. This upshift is ascribed to electron migration from ZnO into the N/O-doped carbon

valence band, which suppresses recombination by spatially separating carriers. The observation corroborates strong interfacial coupling via C–O→Zn and C=N→Zn linkages within the composite.

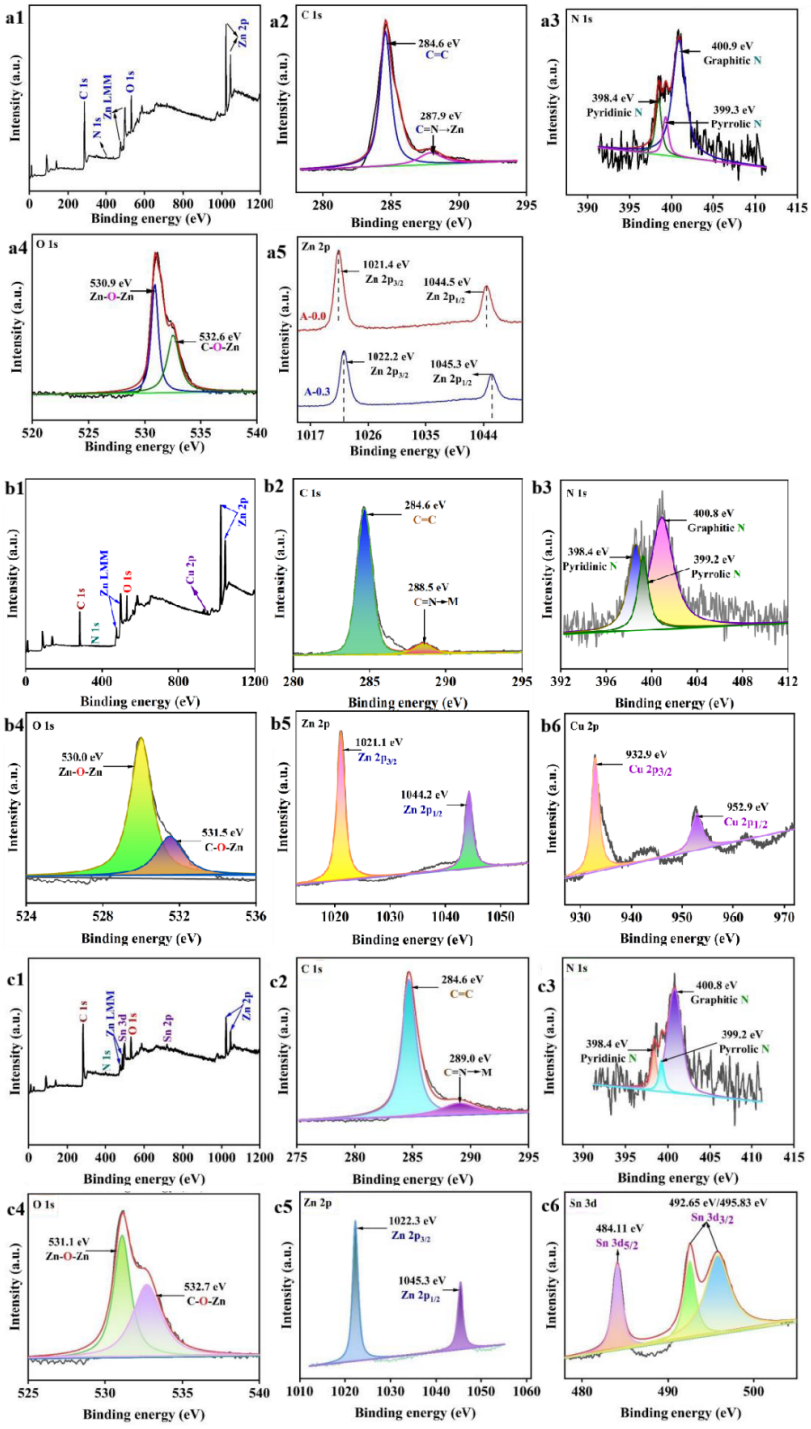

Figure 3 XPS spectra of samples

The XPS survey of CuZ/NOC-9.0% (Fig. 3b) evidences C, N, O, Cu and Zn on the surface. Deconvoluted C 1s emission (Fig. 3b2) yields components at 284.6 eV (C=C) and 288.5 eV (C=N). The N 1s region (Fig. 3b3) is resolved into pyridinic (398.4 eV), pyrrolic (399.2 eV) and graphitic (400.8 eV) nitrogen environments. The O 1s envelope (Fig. 3b4) splits into 530.0 eV (Zn–O–Zn lattice) and 531.5 eV (C–O–Zn interfacial) contributions.

Metallic Cu is confirmed by Cu $2p_{3/2}$ (932.9 eV) and Cu $2p_{1/2}$ (952.9 eV) (Fig. 3b6), while Zn $2p_{3/2}$ and $2p_{1/2}$ appear at 1021.1 eV and 1044.2 eV (Fig. 3b5). Collectively, the data establish the coexistence of all five elements and attest to intimate electronic coupling among ZnO, Cu^0 and NOC—an interaction that accelerates charge separation and boosts photocatalytic activity.

XPS profiling of the Sn-bearing hybrid (Fig. 3c) evidences five surface elements: C, N, O, Sn and Zn.

C 1s line (Fig. 3c2): 284.6 eV (sp^2 C=C) and 289.0 eV (C=N→M).

N 1s line (Fig. 3c3): pyridinic-N 398.4 eV, pyrrolic-N 399.4 eV, graphitic-N 400.9 eV.

O 1s line (Fig. 3c4): 531.1 eV (Zn–O–Zn) and 532.7 eV (C–O–Zn).

Sn 3d line (Fig. 3c6): $3d_{5/2}$ 486.2 eV, $3d_{3/2}$ 494.8 eV → Sn^{4+}.

Zn 2p line (Fig. 3c5): $2p_{3/2}$ 1022.3 eV, $2p_{1/2}$ 1045.3 eV → Zn^{2+}.

Therefore, the XPS results of the sample indicate the existence and chemical states of the five elements and a strong interaction among the three components of ZnO, Sn^0, and NOC in the composite.

3.4 BET Analysis

N_2-physisorption isotherms for T-600, 700 and 800 (Fig. 4a) are all of Type IV, characteristic of mesoporosity [35,36]. Both BET area and pore volume rise up to 700 °C, then decline at 800 °C, revealing a temperature-dependent maximum. At 700 °C the composite reaches its maximum BET area (119.29 $m^2 g^{-1}$) and pore volume (0.060 $cm^3 g^{-1}$). Below this temperature the PS-derived carbon is only partly carbonised, giving weak ZnO–NOC contact and limited porosity; above 700 °C aggressive pyrolysis burns off part of the NOC scaffold, collapsing pores and lowering surface area. N_2 isotherms for A-0.1, 0.3 and 0.5 (Fig. 4b) confirm that the PS/ZnO mass ratio critically tunes porosity. A ratio of 0.30 delivers the highest BET area (119.29 $m^2 g^{-1}$) and pore volume (0.060 $cm^3 g^{-1}$), revealing that an optimum carbon dose templates the desired micro-/meso-structure. This ideal architecture simultaneously broadens light-harvesting, supplies abundant adsorption sites and activates reactant molecules, collectively driving superior photocatalytic activity.

The N_2 adsorption-desorption isotherms of the CuZ/NOC-3.0%~15.0% composite samples are shown in Fig. 4c. This series of composites all exhibited typical Type IV isotherms, indicating a typical mesoporous structure [114]. At a Cu^0:ZnO molar ratio of 9.0 %, CuZ/NOC-9.0 % attains its largest BET area (88.52 $m^2 g^{-1}$), evidencing that a judicious Cu loading markedly boosts both adsorption/activation of reactants and the availability of catalytically active sites.

The specific surface area of the samples was studied through nitrogen adsorption-desorption isotherms (Fig. 4d). The N_2-physisorption isotherms display a Type IV profile, confirming a mesoporous architecture. Varying the Sn^0 molar fraction systematically alters the BET area, which rises to a maximum of 164.81 $m^2 g^{-1}$ at 9.0 % Sn and then declines, attributed to partial volatilization of Sn at elevated pyrolysis temperatures. This optimum Sn level markedly enlarges the surface area, enhancing reactant adsorption/activation and exposing additional active sites, thereby accelerating photocatalytic turnover..

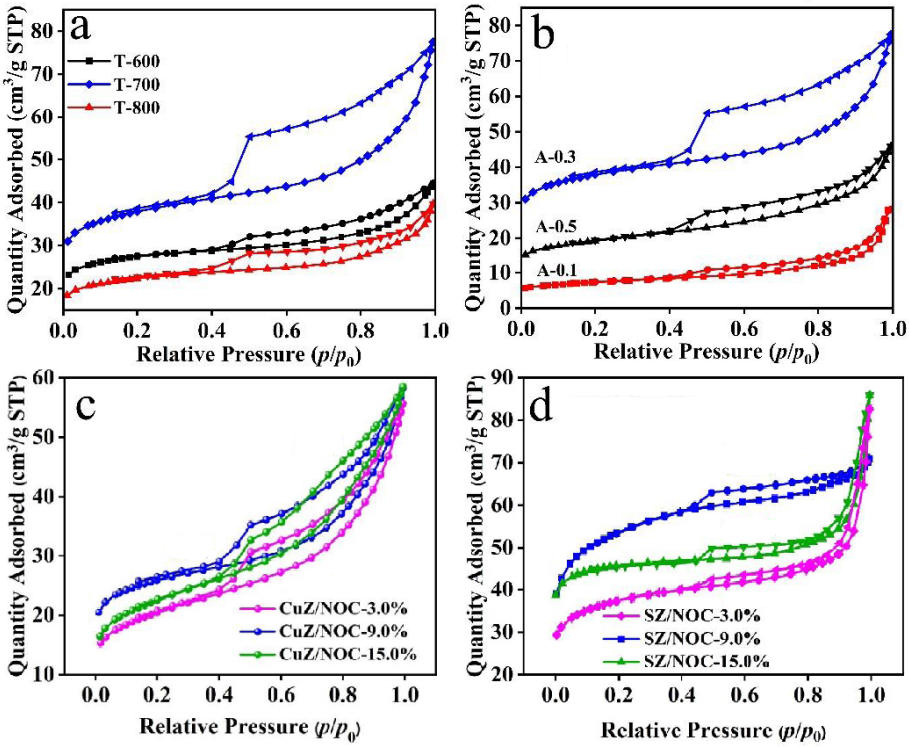

Figure 4 N2 adsorption –desorption curve of samples

3.5 Photocatalytic Performance Study

The optimal A-0.3(T-700) catalyst was tested on MV, MO and TC (10 mg L^{-1} dyes, 30 mg L^{-1} antibiotic) under UV light. Within 28 min the composite removed 98.9 % MB, 96.1 % MV, 83.2 % MO and 89.4 % TC (Fig. 5a). Each run obeyed pseudo-first-order kinetics with k_1 = 0.108, 0.096, 0.071 and 0.086 min^{-1}, respectively (Fig. 5b), evidencing broad-spectrum degradation capability.

To investigate the universality of the composite, under irradiation from a 300W Hg lamp, the best material CuZ/NOC-9.0% was used as the photocatalyst, and MV, MO, and TC solutions were used to simulate other pollutants, as shown in Fig. 5c. It can be found that this composite has excellent adsorption/photocatalytic performance for various organic dyes and tetracycline hydrochloride, with removal rates reaching 98.98% (MB), 91.05% (MV), 80.30% (MO), and 96.39% (TC) within 40 minutes. Meanwhile, fitting its photocatalytic reaction to first-order kinetics, the kinetic constants k_1 were 0.126 min^{-1} (MB), 0.062 min^{-1} (MV), 0.035 min^{-1} (MO), and 0.095 min^{-1} (TC), respectively (Fig. 5d). Therefore, these results fully demonstrate that the prepared CuZ/NOC composite has certain application potential for the removal of organic pollutants.

Given that the composite has excellent adsorption/photocatalytic performance for high-concentration MB solutions, various dyes and tetracycline hydrochloride solutions were used to investigate the universality of the composite. Under irradiation from a 300W Hg lamp, the removal effects of the best composite SZ/NOC-9.0% on MV, MO, and TC solutions are shown in Fig. 5e. Through adsorption and photocatalytic degradation, this composite can effectively remove high-concentration pollutants, achieving removal rates of over 80% for MB, MV, MO (30 mg/L), and TC (50 mg/L) solutions within 25 minutes. This fully proves that the prepared SZ/NOC composite has broad universality for treating various pollutants.

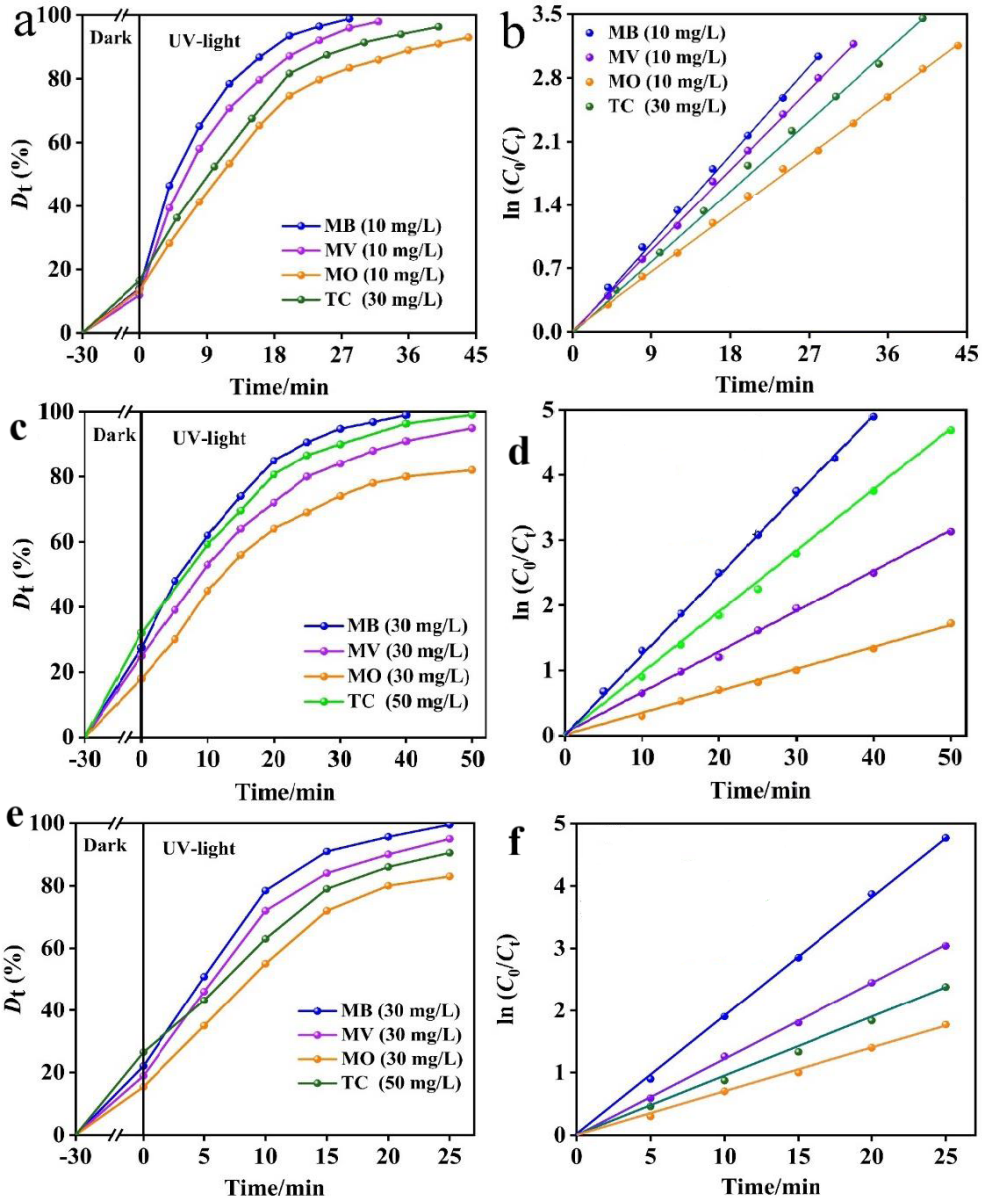

Figure 5 Dt-t and ln (Ct/C0) - t curves and first-order kinetic constants of samples for photocatalytic degradation of different pollutants

3.6 Photocatalytic Mechanism

In the dye adsorption process, the main actions are physical adsorption and π-π interaction working together, belonging to heterogeneous catalysis, but the π-π interaction is more significant [37-38]. π–π stacking between the aromatic systems of the pollutants and the conjugated NOC framework pre-activates the adsorbed molecules, facilitating their subsequent photocatalytic breakdown. Comparable behaviour has been documented elsewhere. Upon visible-light excitation, electrons are promoted from the NOC valence band to its conduction band; simultaneously, electrons transfer from the ZnO valence band into the NOC valence band, generating a spatially separated pair consisting of an electron in the NOC conduction band and a hole in the ZnO valence band. MB, O_2 and H_2O molecules are concurrently adsorbed on the nanocomposite surface. Adsorbed MB (MB-ad) captures electrons from the NOC π-network via π–π coupling, yielding a reduced, activated MB-ad species. Concurrently, surface-adsorbed O_2 accepts CB electrons from NOC to generate $\bullet O_2^-$ radicals, while adsorbed H_2O is oxidized by VB holes in ZnO to produce •OH radicals. The activated MB species

(MB-*ad) are readily mineralized by $\bullet O_2^-$ and •OH radicals, with •OH acting as the dominant oxidant in the process.

Proposed visible-light pathway for the SZ/NOC catalyst: photons excite VB electrons of ZnO into adjacent Sn 5p orbitals lying just below the CB (Eq. 1), leaving holes in the ZnO VB. Photogenerated electrons in the Sn-derived CB level are swiftly injected into the NOC matrix (Eq. 2), stabilizing the charge and suppressing recombination. Meanwhile, MB, O_2 and H_2O adsorb on the nanocomposite; MB-ad accepts electrons from the NOC π-system via π–π coupling to yield activated MB-ad, whereas adsorbed H_2O is oxidized by VB holes in ZnO to produce •OH radicals. Surface-bound O_2 scavenges CB electrons from NOC to yield $\bullet O_2^-$, while the activated MB-*ad species are rapidly mineralized by the combined action of $\bullet O_2^-$ and •OH, with •OH serving as the principal oxidizing species.

4 Conclusion

In short, fine-tuning calcination temperature, biomass loading and the Sn:Zn molar ratio via a solvothermal-calcination route yields Sn–ZnO/NOC ternary hybrids that integrate N/O-doped biochar and exhibit superior adsorption plus UV/visible photocatalytic activity. The biomass reduced Sn^{4+} ions to metallic Sn^0, and the biomass played multiple roles during the experiment: carbon source, template, and reducing agent. After photocatalytic performance testing, the optimal calcination temperature was determined to be 700°C, the mass ratio of PS to metal was 0.30, and the molar ratio of Sn to ZnO was 9.0%. After a series of characterizations, the results showed that the large specific surface area provided more active sites. Electrochemical analysis revealed that incorporating Sn markedly modifies the electronic framework, substantially lowering charge-transfer resistance. From TPR and fluorescence spectra, it can be seen that the photocurrent density of the composite was greater than that of other components, indicating higher separation efficiency of photogenerated carriers in the composite. The fluorescence intensity was lower than that of Z/NOC and ZnO, indicating that the introduction of Sn inhibited the recombination of photogenerated carriers in the material. Photocatalytic screening demonstrated rapid UV-driven degradation of diverse organic pollutants, underscoring the composite's broad-spectrum degradation capability. Under visible light and sunlight irradiation, the composite can effectively decompose MB and TC, indicating its certain practicality. Radical-scavenging tests identified •OH, $\bullet O_2^-$ and h^+ as the key oxidative agents; among them, •OH exerts the dominant influence on MB degradation. Additionally, the catalyst also exhibited excellent stability. Therefore, the Sn@ZnO/NOC photocatalyst prepared in this experiment overcomes the main defects of ZnO. The introduction of Sn metal and biomass has a positive impact on its modification, and the interaction among the three is the main factor for improving its catalytic activity. This catalyst uses waste biomass as raw material, has a simple preparation method, and possesses certain universality, practicality, and stability, showing potential application value.

References

[1] Rasheed H S, Ahmed N M, Matjafri M Z, et al. Multilayer ZnO/Pd/ZnO Structure as Sensing Membrane fo r Extended-Gate Field-Effect Transistor (EGFET) with High pH Sensitivity[J]. Journal of Electronic Materials, 2017, 4610: 5901-5908.

[2] Pei G X, Wijten J H J and Weckhuysen B M. Probing the dynamics of photogenerated holes indoped hemat ite photoanodes for solar water splitting using transient absorption spectroscopy[J]. Phys Chem Chem Ph ys, 2018, 2015: 9806-9811.

[3] Dash P, Manna A, Mishra N C, et al. Synthesis and characterization of aligned ZnO nanorods for visible ligh t photocatalysis[J]. Physica E: Low-dimensional Systems and Nanostructures, 2019, 107: 38-46.

[4] Martino G A, Piovano A, Barzan C, et al. Cr[CH(SiMe3)2]3/SiO2 catalysts for ethene polymerization: The co rrelation at a molecular level between the chromium loading and the microstructure of the produced pol ymer[J]. Journal of Catalysis, 2021, 394: 131-141.

[5] Kumar K V A, Amanchi S R, Sreedhar B, et al. Phenol and Cr(VI) degradation with Mn ion doped ZnO under visible light photocatalysis[J]. RSC Advances, 2017, 768: 43030-43039.

[6] Yasin M, Saeed M, Muneer M, et al. Development of Bi2O3-ZnO heterostructure for enhanced photodegr adation of rhodamine B and reactive yellow dyes[J]. Surfaces and Interfaces, 2022, 30: 101846-101849.
[7] Zheng X, Zhang H, Liu M, et al. Porous sponge with surface modified for superhydrophobic/superoleophili c and special functionalization[J]. Journal of Polymer Research, 2022, 296: 237-244.
[8] Saravanan A, Kumar P S, Vo D-V N, et al. Photocatalysis for removal of environmental pollutants and fuel production: a review[J]. Environmental Chemistry Letters, 2020, 191: 441- 463.
[9] Truong T K, Van Doan T, Tran H H, et al. Effect of Cr Doping on Visible-Light-Driven Photocatalytic Activity of ZnO Nanoparticles[J]. Journal of Electronic Materials, 2019, 4811: 7378-7388.
[10] Gwenzi W, Chaukura N, Noubactep C, et al. Biochar-based water treatment systems as a potential low-co st and sustainable technology for clean water provision[J]. J Environ Manage, 2017, 197: 732-749.
[11] Baskoutas S. Special Issue: Zinc Oxide Nanostructures: Synthesis and Characterization[J]. Materials, 2018, 116: 873-878.
[12] Hendrix D, McKeon J and Wille K. Behavior of Colloidal Nanosilica in an Ultrahigh Performance Concrete E nvironment Using Dynamic Light Scattering[J]. Materials, 2019, 1212: 1976-1980.
[13] Wu J, Liu J, Wen B, et al. Nitrogen-rich covalent triazine frameworks for high-efficient removal of anion dy es and the synergistic adsorption of cationic dyes[J]. Chemosphere, 2021, 272: 129622-129627. [28] Giris h Kumar S and Kavitha R. Lanthanide ions doped ZnO based photocatalysts[J]. Separation and Purification Technology, 2021, 274: 118853-118859.
[14] Ilnytskyi J M, Slyusarchuk A and Sokolowski S. Gelation of patchy ligand shell nanoparticles decorated by l iquid-crystalline ligands: computer simulation study[J]. Soft Matter, 2018, 1419: 3799-3810.
[15] Chen M, Bao C, Hu D, et al. Facile and low-cost fabrication of ZnO/biochar nanocomposites from jute fiber s for efficient and stable photodegradation of methylene blue dye[J]. Journal of Analytical and Applied Py rolysis, 2019, 139: 319-332.
[16] Shahrbaf M A, Akbarzadeh M A, Tabary M, et al. Air Pollution and Cardiac Arrhythmias: A Comprehensive Review[J]. Curr Probl Cardiol, 2021, 463: 100649-100652.
[17] Gavrilescu M, Demnerova K, Aamand J, et al. Emerging pollutants in the environment: present and future challenges in biomonitoring, ecological risks and bioremediation[J]. N Biotechnol, 2015, 321: 147-156.
[18] Meng Y, Zhang X, Pan G, et al. Orthogonal synthesis of a novel hybrid layered material containing three di fferent zincous components and its photocatalytic property investigation[J]. J Hazard Mater, 2018, 350: 1 44-153.
[19] Hong D H, Reddy D A, Reddy K A J, et al. Synergetic catalytic behavior of dual metal-organic framework co ated hematite photoanode for photoelectrochemical water splitting performance[J]. Journal of Catalysis, 2020, 391: 471-479.
[20] Segovia M, Alegría M, Aliaga J, et al. Heterostructured 2D ZnO hybrid nanocomposites sensitized with cub ic Cu2O nanoparticles for sunlight photocatalysis[J]. Journal of Materials Science, 2019, 5421: 13523-1353 6.
[21] Mishra M, Chun D M. α-Fe2O3 as a photocatalytic material: A review[J]. Applied Catalysis A: General, 201 5, 498: 126-141.
[22] Yang L, Ding R, Hong C, et al. Synthesis, optical and photocatalysis property of ZnO:Tb nanoparticles[J]. So lid State Sciences, 2022, 131: 225-234.
[23] Gubanova E, Schmidt T O, Watzele S, et al. Structure-Dependent Electrical Double-Layer Capacitances of t he Basal Plane Pd(hkl) Electrodes in HClO4[J]. The Journal of Physical Chemistry C, 2022, 12627: 11414-11 420.
[24] Bourkeb K W and Baaloudj O. Facile electrodeposition of ZnO on graphitic substrate for photocatalytic ap plication: degradation of antibiotics in a continuous stirred-tank reactor[J]. Journal of Solid State Electroc hemistry, 2021, 262: 573-580.
[25] Zhang F, Peng H, Jiang S, et al. Construction of precious metal-loaded BiOI semiconductor materials with i mproved photocatalytic activity for microcystin-LR degradation[J]. Environ Sci Pollut Res Int, 2019, 268: 8 226-8236.
[26] Fernandez V, Morgan D, Bargiela P, et al. Combining PCA and nonlinear fitting of peak models to re-evalu ate C 1s XPS spectrum of cellulose[J]. Applied Surface Science, 2023, 614: 156182- 156188.
[27] Lazar P, Mach R and Otyepka M. Spectroscopic Fingerprints of Graphitic, Pyrrolic, Pyridinic, and Chemisor bed Nitrogen in N-Doped Graphene[J]. The Journal of Physical Chemistry C, 2019, 12316: 10695-10702.
[28] Ma J, Wang X, Zong X, et al. Photoelectrochemical properties of TiO2/g-C3N4 composited electrodes fabri cated by a co-electrodeposited method[J]. Journal of Physics D: Applied Physics, 2021, 5414: 1361-6463.

[29] [112] Nisha V, Moolayadukkam S, Paravannoor A, et al. Cu doped graphitic C3N4 for p-nitrophenol reduct ion and sensing applications[J]. Inorganic Chemistry Communications, 2022, 142: 109598-109600.
[30] Lu X, Kanamori K and Nakanishi K. Preparation of zinc oxide with a three-dimensionally interconnected m acroporous structure via a sol-gel method accompanied by phase separation[J]. New Journal of Chemistr y, 2019, 4329: 11720-11726.
[31] Chen H-Y and Chen P-C. P-type spinel ZnCo2O4 thin films prepared using sol-gel process[J]. Applied Surfac e Science, 2020, 505: 144460-144466.
[32] Wang C L, Zhou G, Ma K, et al. Research on damage of typical water-containing composite structure unde r different types of charge[J]. Journal of Physics: Conference Series, 2020, 15073: 032066-032069.
[33] Tang C, Chen C, Zhang H, et al. Enhancement of degradation for nitrogen doped zinc oxide to degrade me thylene blue[J]. Physica B: Condensed Matter, 2020, 583: 412029-412034.
[34] Ma X, Li S, Qu Z, et al. A highly active Z-scheme NiGa2O4/anthraquinone/MoO3 photocatalyst via charge t ransfer for sunlight photocatalytic simultaneous conversions of nitrite and sulfite[J]. Journal of Industrial a nd Engineering Chemistry, 2019, 78: 303-314.
[35] Yu F, Gong F, Yang Q, et al. Fabrication of a magnetic retrievable dual Z-scheme g- C3N4/BiVO4/CoFe2O4 composite photocatalyst with significantly enhanced activity for the degradation of rhodamine B and hyd rogen evolution under visible light[J]. Diamond and Related Materials, 2022, 125: 109004-109008.
[36] Brunckova H, Kanuchova M, Kolev H, et al. XPS characterization of SmNbO4 and SmTaO4 precursors prep ared by sol-gel method[J]. Applied Surface Science, 2019, 473: 1-5.
[37] Rasheed T, Bilal M, Nabeel F, et al. Environmentally-related contaminants of high concern: Potential sourc es and analytical modalities for detection, quantification, and treatment[J]. Environ Int, 2019, 122: 52-66.
[38] Ge H, Xu G, Huang J, et al. A mine main fans switchover system with lower air flow volatility based on imp roved particle swarm optimization algorithm[J]. Advances in Mechanical Engineering, 2019, 113: 3-9.
[39] Hwang J S, Lin Y H, Hwang J Y, et al. Imaging layer number and stacking order through formulating Raman fingerprints obtained from hexagonal single crystals of few layer graphene[J]. Nanotechnology, 2013, 241: 15702-.15712
[40] Leichtweis J, Silvestri S and Carissimi E. New composite of pecan nutshells biochar-ZnO for sequential rem oval of acid red 97 by adsorption and photocatalysis[J]. Biomass and Bioenergy, 2020, 140: 105648-10565 6.